EES Batteries

PAPER

View Article Online
View Journal | View Issue

Cite this: *EES Batteries*, 2025, **1**, 1785

Structural polymorphism and carrier effects in sodium-ion conducting Prussian blue-type solid electrolytes

Taewon Kim,†[a] You-Yeob Song,†[b] Seungwoo Ryu,†[c] Sang Hyeok Ahn,[c] Beom Jin Park,[c] Chanhee Lee,[c] Min-Ho Kim,[d] Dong-Hwa Seo, *[b] Sung-Kyun Jung *[c] and Hyun-Wook Lee *[c]

Prussian blue analogues are renowned for their open-framework structures composed of CN^- ligands, which distinguish them from conventional solid electrolyte materials. This study explores the effects of mobile carrier concentrations, water content, and structural integrity on the performance of solid electrolytes in all-solid-state batteries. By analyzing different phases of manganese hexacyanoferrate: cubic, monoclinic, and rhombohedral, we correlate Na^+ and water content with lattice distortions and Na^+ conductivity. Computational simulations corroborate experimental findings on activation energies and coulombic interactions between Na^+ and CN^- ligands, taking into account carrier concentrations and structural polymorphism. The cubic phase, exhibiting lower Na^+ content and comparable water content to the monoclinic phase, demonstrates the fastest Na^+ migration and the lowest activation energy. In terms of cell performance, the higher Na^+ content of the monoclinic phase enhances cycling performance by reducing the chemical potential difference between manganese hexacyanoferrate and the anode. Monoclinic manganese hexacyanoferrate-based solid-state batteries enable stable cycling performance of the $Na_2Mn[Mn(CN)_6]$ cathode, with discharge capacities of 60 mAh g^{-1} using a Mn(I)/Mn(II) redox couple at room temperature and 120 mAh g^{-1} using dual redox couples of Mn(I)/Mn(II) and Mn(II)/Mn(III) at 30 °C. This study underscores the critical role of Na^+ and water content in optimizing Na^+ conductivity and overall battery performance.

Received 9th July 2025,
Accepted 5th August 2025

DOI: 10.1039/d5eb00129c

rsc.li/EESBatteries

Broader context

Conventional solid electrolyte frameworks containing sulphur (S^{2-}), oxygen (O^{2-}), chlorine (Cl^-), bromine (Br^-), or iodine (I^-) anions present serious limitations. Sulfide-based electrolytes lead to the evolution of toxic H_2S gas; oxide electrolytes suffer from poor interparticle contact and require high-temperature sintering (>900 °C); and halide electrolytes often rely on rare and expensive materials like Y, In, and Sc. Considering these obstacles, we explore Prussian blue analogues (PBAs) as alternative solid electrolytes composed of CN^- anions. These analogues not only are more affordable due to inexpensive elements and cost-effective synthesis methods, but they also maintain stability in air. PBAs allow for the manipulation of intrinsic parameters, such as mobile carrier concentrations, water content, and structural integrity, all of which are critical for their performance as solid electrolytes. In this study, we investigate the effects of these parameters on the performance of PBAs in all-solid-state sodium batteries. Specifically, we analyze different phases of manganese hexacyanoferrate (cubic, monoclinic, and rhombohedral), focusing on variations in Na^+ and water content and their impact on lattice distortion and Na^+ conductivity. Our results highlight the essential role of Na^+ and water content in optimizing ionic conductivity and enhancing battery performance.

Introduction

The growing demand for energy storage solutions across diverse applications has intensified the search for alternative battery technologies due to a significant increase in the cost of lithium resources, including cobalt, nickel, vanadium, and lithium ores.[1–6] Consequently, alternatives such as all-solid-state sodium (Na^+) batteries (ASNBs) have gained increasing importance. Sodium batteries offer notable advantages, including lower overall costs and the greater abundance of

[a]*Department of Materials, University of Oxford, Oxford OX13PH, UK*
[b]*Department of Materials Science and Engineering, Korea Advanced Institute of Science and Technology (KAIST), Daejeon 34141, Republic of Korea. E-mail: dseo@kaist.ac.kr*
[c]*School of Energy and Chemical Engineering, Ulsan National Institute of Science and Technology (UNIST), Ulsan 44919, Republic of Korea. E-mail: skjung@unist.ac.kr, hyunwooklee@unist.ac.kr*
[d]*Department of Chemical and Biomolecular Engineering, University of California, Los Angeles, California 90095, USA*
†These authors contributed equally to this work.

sodium, which is less susceptible to sharp cost fluctuations.[7–11] Therefore, ASNBs utilizing nonflammable solid electrolytes have attracted considerable attention, offering enhanced safety and leveraging the low cost and abundance of Na resources.[12,13] A critical factor in the success of ASNBs is the development of solid electrolytes with high ionic conductivity, chemical stability, and compatibility with both electrodes.[14–19]

Intensive research on sodium ion conducting solid electrolytes has led to significant advancements in identifying various candidates, including oxides (*e.g.*, $Na_3Zr_2Si_2PO_{12}$, 0.67 mS cm^{-1}),[20] sulfides (*e.g.*, Na_3SbS_4, 1 mS cm^{-1}),[21,22] and halides (*e.g.*, Na_2ZrCl_6, 0.018 mS cm^{-1}).[23] While these solid electrolytes demonstrate high ionic conductivity and potential for practical applications, they face critical commercialization challenges related to fabrication protocols, material costs, and chemical stability. For example, sulfide-based solid electrolytes suffer from poor air and chemical stability, leading to the evolution of toxic H_2S gas and a narrow voltage window, which limits their utilization as solid electrolytes.[22,24] Oxide-based solid electrolytes require high-temperature sintering processes to reduce grain boundaries and improve Na ionic conductivity due to poor ionic contact between particles.[20,25,26] Halide-based solid electrolytes are composed of expensive and rare materials, such as Y, Er, and Sc, paired with halide ions, which increases their cost and results in instability in low voltage ranges below 1 V.[24,27] Furthermore, the typical synthesis methods for solid electrolytes, such as solid-solution or ball-milling techniques, are not suitable for large-scale commercialization.[14,28,29] Considering these significant challenges, Prussian blue analogue (PBA)-based solid electrolytes have emerged as promising alternatives to traditional solid electrolytes because they offer several advantages, including the use of inexpensive elements, cost-effective synthesis methods, and stability in air.[10,30]

A distinctive feature of PBAs is their ability to exhibit structural polymorphism, significantly influencing their physical and chemical properties. In the context of Prussian blue-type solid electrolytes, this structural polymorphism can influence ionic conductivity and overall battery performance. Typically, PBAs adopt a cubic structure, but depending on the number of vacancies in the $R(CN)_6$ compounds, the crystal structure can distort to monoclinic, orthorhombic, or rhombohedral forms. These variations in crystal structures result in different electrochemical behaviors when used as electrode materials.[31,32] Therefore, understanding and controlling the structural polymorphism in PBAs is crucial for optimizing their function as solid electrolytes in ASNBs as well. Moreover, a key factor influencing the performance of Prussian blue-type solid electrolytes is the concentration of mobile cations, such as sodium ions, within the crystal lattice. The synthetic conditions, particularly the concentration of sodium precursors during synthesis, can vary the amount (x) of sodium cations from zero to two, as per the chemical formula $Na_xP[R(CN)_6]$. The distribution and dynamics of these ions are closely linked to the specific structural polymorphs present in the material. Different polymorphs may exhibit varying degrees of openness in their frameworks, which can either facilitate or hinder ion migration. Consequently, a comprehensive investigation into the relationship between structural polymorphism and mobile cation concentration is essential for designing high-performance sodium-ion conducting solid electrolytes. In this study, we investigate a representative Prussian blue-type solid electrolyte, manganese hexacyanoferrate (MnHCFe), in its different crystallographic phases: cubic, monoclinic, and rhombohedral (Fig. 1a–c). These phases correlate with the Na^+ and water content. The intrinsic features, such as sodium (Na^+) mobile carrier concentration, water content, and structural integrity, can be critical variables for the performance of solid electrolytes in ASNBs. For example, changes in bonding covalency, influenced by the number of structural water molecules, impact the structural vibration energy, which contributes to the temperature coefficients of PBA structures.[31] The presence of interstitial water molecules surrounding the transition-metal ions can enhance the effect of coordinated water, leading to variations in the direction of cyanide ligand stretching. This characteristic offers a unique advantage compared to other conventional solid electrolytes, such as those based on sulphur (S^{2-}), oxygen (O^{2-}), chlorine (Cl^-), bromine (Br^-), or iodine (I^-) anions. Computational simulations are crucial for validating the activation energies and coulombic interactions between Na^+ and CN^- ligands, considering carrier concentrations and structural polymorphism. The cubic phase, which has lower Na^+ and comparable water content to the monoclinic phase, is expected to exhibit fast Na^+ migration and low activation energy due to minimal coulombic attraction, unlike the rhombohedral phase. Fundamental analysis allows comparison of the three MnHCFe solid-electrolyte phases in ASNBs. Benefiting from the aforementioned features, the cubic and monoclinic phases are expected to enhance ionic conductivity by reducing the chemical potential difference between MnHCFe and the anode, thereby leading to stable cycling performance. Solid-state batteries using the monoclinic MnHCFe solid electrolyte can be expected to demonstrate stable cycling performance with manganese hexacyano-manganate ($Na_2Mn[Mn(CN)_6]$, MnHCMn) as a cathode material. This study expands on the considerable Na^+-ion conducting mechanisms that play a critical role in governing the kinetics and stability of overall battery performance in ASNBs, providing valuable insights for new electrolyte design.

Results and discussion

Characterization of the three MnHCFe phases

To elucidate the relationship between the structure of MnHCFe and the concentrations of Na^+ and water molecules, we conducted a detailed chemical composition and structural characterization study of the three MnHCFe crystal structures. These structures were varied in terms of Na^+ and water content and synthesized using a co-precipitation method optimized for temperature, aging time, and drying conditions. The chemical

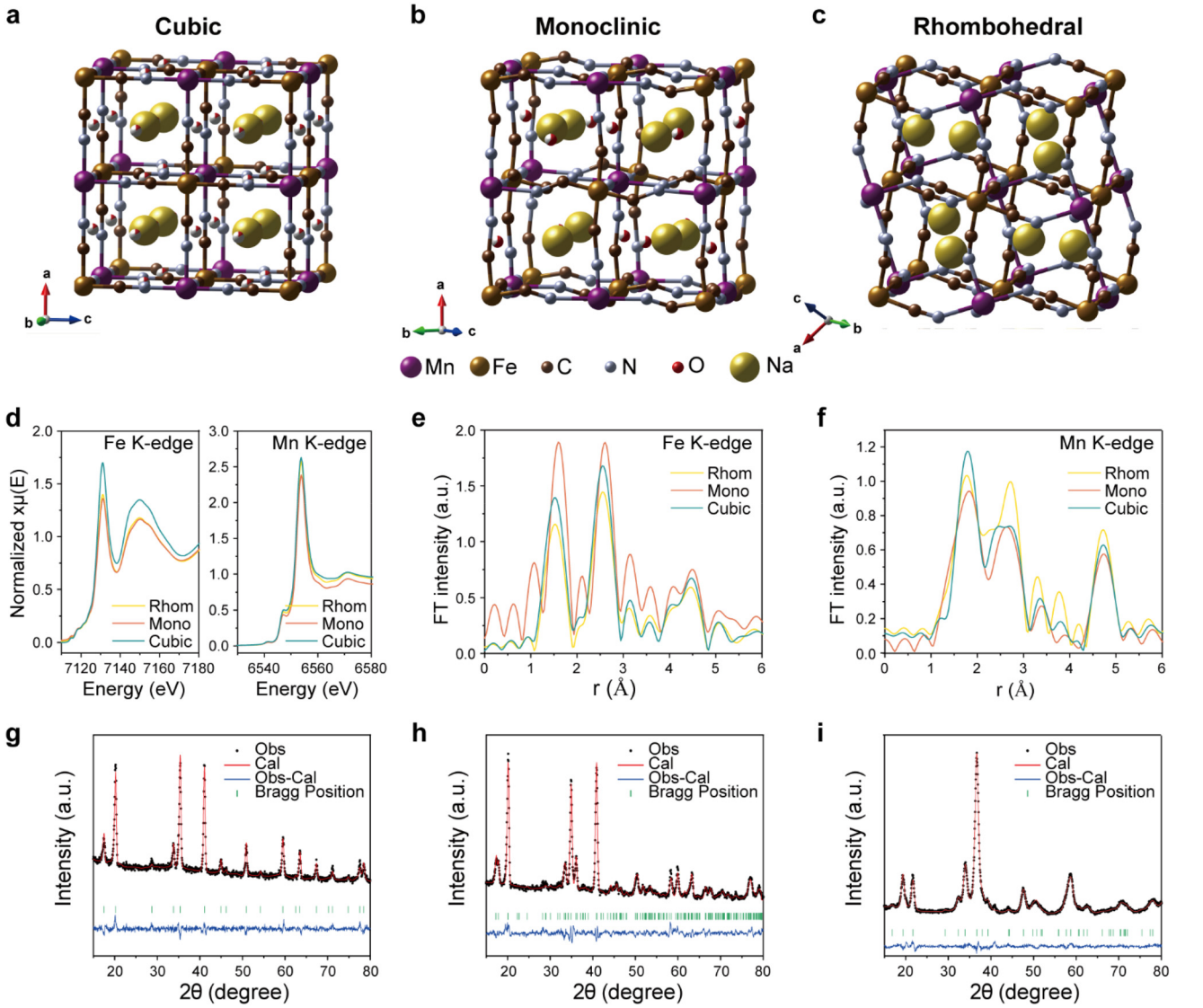

Fig. 1 Structural characterization of MnHCFe with varying crystal structures. Schematic illustrations of the unit cell structure of MnHCFe in (a) cubic, (b) monoclinic, and (c) rhombohedral crystal phases. (d) XANES spectra for the Fe K-edge (left panel) and Mn K-edge (right panel). (e and f) EXAFS analysis for Fe K-edge (e) and Mn K-edge (f). Neutron powder diffraction patterns of MnHCFe in (g) cubic, (h) monoclinic, and (i) rhombohedral phases. The diffraction patterns confirm the phase crystallinity of the samples.

compositions of the cubic, monoclinic, and rhombohedral MnHCFe structures, determined through ICP-MS and TGA, are listed as $Na_{1.04}Mn[Fe(CN)_6]_{0.80}\cdot 1.04H_2O$, $Na_{1.51}Mn[Fe(CN)_6]_{0.93}\cdot 1.49H_2O$, and $Na_{1.51}Mn[Fe(CN)_6]_{0.91}\cdot 0.16H_2O$, respectively, as shown in Fig. S1 and Table S1. Scanning electron microscopy analysis revealed similar cubic morphologies and sizes for all samples (Fig. S2). X-ray absorption near-edge spectroscopy (XANES) and extended X-ray absorption fine structure (EXAFS) at the Fe K-edge and Mn K-edge, coupled with neutron powder diffraction (NPD), confirmed the oxidation states of Fe and Mn as +2,[33,34] with main peaks at 7130 eV and 6553 eV, respectively, suggesting identical initial oxidation states across the samples (Fig. 1d). The EXAFS analyses indicated Fe–C and Fe–N distances of about 2 Å and 3 Å, respectively (Fig. 1e and f).[33,34] NPD and subsequent Rietveld refinement provided further structural insights, revealing that each MnHCFe sample exhibited distinct cubic, monoclinic, and rhombohedral phases (Fig. 1g–i and Tables S2–S5). A detailed examination validates that the MnHCFe samples with a higher interstitial Na^+ content exhibit greater lattice distortions, particularly notable when comparing the cubic structure containing a Na^+ ratio of 1 in the composition of $Na_xMn[Fe(CN)_6]$ and the monoclinic and rhombohedral structures containing a Na^+ ratio of 1.5. Regarding water content, lower water content is also associated with increased lattice distortions, as seen in the monoclinic MnHCFe containing 1.49 mol of H_2O compared to the rhombohedral structure with only 0.16 mol of H_2O. These structural changes are likely driven by the

interactions between Na^+ ions and the N^- ions in CN^- ligands. As previously reported by Henkelman *et al.*, intercalated Na^+ ions engage in Coulomb attraction with N^- ions, and the strength of this attraction varies with the amounts of Na^+ and water molecules, influencing the structural dynamics of MnHCFe.[35] Consequently, a higher Na^+ content leads to more significant lattice distortions, potentially transitioning a cubic structure to a monoclinic and further to a rhombohedral structure as the water content decreases. These interactions also suggest that higher Na^+ and lower water content may induce slower Na^+-ion conduction in MnHCFe by increasing the activation energy for Na^+ migration. These findings deepen our understanding of Na^+ migration in PBA solid electrolytes and underscore the critical role of structural and compositional variables in optimizing their performance.

Na^+ tuning of phase and ionic transport

To establish a more detailed correlation between Na^+ concentration and ionic conductivity, we prepared MnHCFe samples with varying Na^+ contents and characterized their structural properties using ICP-MS and TGA. The chemical compositions of these samples were determined as $Na_{0.66}Mn[Fe(CN)_6]_{0.70}\cdot 1.63H_2O$, $Na_{0.74}Mn[Fe(CN)_6]_{0.73}\cdot 1.77H_2O$, $Na_{1.00}Mn[Fe(CN)_6]_{0.81}\cdot 1.95\ H_2O$, $Na_{1.10}Mn[Fe(CN)_6]_{0.83}\cdot 1.87H_2O$, and $Na_{1.29}Mn[Fe(CN)_6]_{0.88}\cdot 1.99H_2O$, as shown in Fig. S3 and Table S6. Synchrotron X-ray diffraction (XRD) patterns were analyzed *via* Le Bail fitting (Fig. 2a and Table S7) to investigate how variations in Na^+ content influence structural transitions. The results indicate that MnHCFe retains a cubic structure when the Na^+ content is below 1.00. However, a Na^+ content exceeding 1.00 initiates a phase transition to the monoclinic structure. Additionally, electrochemical impedance spectroscopy (EIS) was performed on Na^+-blocking symmetric cells to examine the ionic conductivity of these MnHCFe samples as a function of Na^+ content (Fig. 2b and Fig. S4). The results validate that ionic conductivity steadily increases within the cubic phase as Na^+ content increases, peaking at a Na^+ content of 1.00. Beyond this threshold, the transition to the monoclinic phase results in a sharp decrease in ionic conductivity. This trend highlights the critical role of structural transitions in determining Na^+ transport properties, with the cubic phase facilitating superior ion conduction compared to the monoclinic phase. Furthermore, Fig. 2c illustrates that in the cubic phase, both the lattice parameter and ionic conductivity increase with Na^+ content, indicating a correlation between Na^+ content and lattice expansion. Specifically, the lattice parameter reaches 10.480 Å at a Na^+ content of 1.00. This expansion provides wider pathways for Na^+ migration, significantly enhancing ionic conductivity.[36,37] Arrhenius plots in Fig. S5 further reveal that activation energy decreases while ionic conductivity increases within the cubic phase (Na^+ content of 0.66 to 1.00). Beyond a Na^+ content of 1.00, the phase transition to the monoclinic phase leads to a sharp increase in activation energy, making Na^+ migration more difficult. These results demonstrate that an increase in Na^+ content expands the channel size of cubic MnHCFe, thereby enhancing ionic conductivity. However, the transition to the monoclinic phase beyond a Na^+ content of 1.00 restricts Na^+ migration, resulting in reduced ionic conductivity.

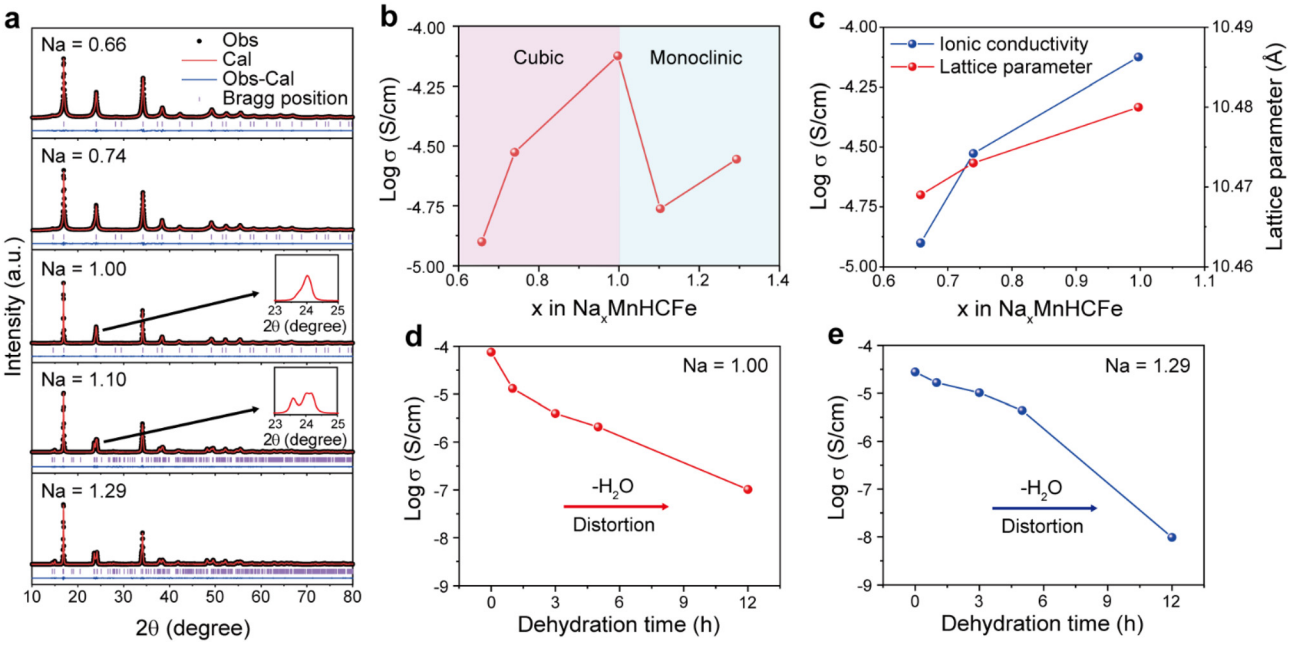

Fig. 2 Na^+ and water-dependent structural and ionic conductivity of MnHCFe. (a) Synchrotron X-ray diffraction patterns of MnHCFe with different amounts of Na^+. (b) Ionic conductivity of MnHCFe as a function of Na^+ content at 30 °C. (c) Lattice parameter and ionic conductivity as a function of Na^+ content in cubic MnHCFe. Ionic conductivity of MnHCFe at 30 °C as a function of dehydration time at 70 °C for pristine (d) cubic and (e) monoclinic MnHCFe.

Water content effect on the structure and ionic transport

The presence of water molecules in the lattice also plays a critical role in determining structural stability and ionic conductivity. To investigate the effect of water removal, synchrotron XRD, Le Bail fitting, and EIS analyses were conducted to examine these transitions. As shown in Fig. 2d, MnHCFe with a Na^+ content of 1.00, which initially adopts a cubic phase, experiences a progressive decline in ionic conductivity during dehydration at 70 °C. This is attributed to the gradual removal of lattice water molecules, which induces structural distortions and destabilizes the cubic phase, leading to a distorted monoclinic phase (Fig. S6 and Table S8) and reduced ionic conductivity (Fig. S7). After 12 hours of dehydration, the structure transitions into a highly distorted monoclinic phase with the β angle exceeding 101°, resulting in the loss of ionic conductivity. Similarly, Fig. 2e illustrates the effects of dehydration on MnHCFe with a Na^+ content of 1.29, which initially exhibits a monoclinic phase. In this case, the ionic conductivity decreases as water is removed, with the monoclinic phase becoming increasingly distorted (increasing β angle) under dehydration conditions and eventually transitioning into the rhombohedral phase (Fig. S8 and Table S9), further hindering Na^+ conduction (Fig. S9). These observations suggest that the removal of water molecules disrupts structural stability and reduces ionic conductivity, with phase transitions hindering Na^+ migration.

Elucidation of Na^+ migration barriers across different phases

To validate the correlation between Na^+ migration and the concentrations of Na^+/H_2O, we employed EIS analysis on SUS/MnHCFe/SUS symmetric cells for three representative MnHCFe phases: cubic ($Na_{1.04}Mn[Fe(CN)_6]_{0.80}\cdot 1.04H_2O$), monoclinic ($Na_{1.51}Mn[Fe(CN)_6]_{0.93}\cdot 1.49H_2O$), and rhombohedral ($Na_{1.51}Mn[Fe(CN)_6]_{0.91}\cdot 0.16H_2O$). As shown in Fig. S10, the Na^+ conductivities of the cubic, monoclinic, and rhombohedral phases of MnHCFe at 30 °C are found to be 8.3×10^{-2} mS cm^{-1}, 2.2×10^{-2} mS cm^{-1}, and 6.1×10^{-5} mS cm^{-1}, respectively. Additionally, we conducted a combined characterization study on impedance using distribution of relaxation time (DRT) and equivalent circuit model fitting analysis (Fig. S11) on the cubic and monoclinic MnHCFe phases as shown in Fig. 3a and b and Tables S10 and S11.[38,39] For the rhombohedral MnHCFe, which possessed high impedance, an equivalent circuit fit was employed instead of DRT analysis to obtain more reliable data (Table S12). This approach allows us to isolate variables such as grain boundary impedance and ohmic resistance. This separation enhances the understanding of the intricate relationship between Na^+ migration and the structural characteristics of the MnHCFe phases. Fig. 3a and b show the DRT results for the cubic and monoclinic MnHCFe exhibiting deconvoluted peaks corresponding to bulk and grain boundary contributions. Fig. 3c shows the bulk intrinsic activation energies for Na^+ migration in the three MnHCFe phases. The activation energies are determined to be 0.42 eV for cubic, 0.49 eV for monoclinic, and 0.84 eV for rhombohedral phases, aligning with the expected trend previously discussed in the structural analysis section. These results underscore that the cubic phase, with the lowest activation energy, facilitates easier Na^+ migration, whereas the rhombohedral phase, with higher interaction between Na^+ and CN^- ligands, possesses the largest activation energy, influenced by the varying amounts of Na^+ and water.

To complement the relationship between Na^+ migration and the interactions between Na^+ and CN^- ligands, we fabricated ASNBs using rhombohedral MnHCFe as solid electrolyte, in states before and after humid air exposure, $Na_2Mn[Mn(CN)_6]$ (MnHCMn) as the cathode, and Na_3Sn as the anode. Initial tests with rhombohedral MnHCFe revealed no Na^+ conduction or redox reactions, as confirmed by EIS and cyclic voltammetry (CV) measurements (Fig. S12 and S13). However, exposure of rhombohedral MnHCFe to humid air (80% relative humidity) for 24 hours resulted in a phase transition to a monoclinic structure. This altered phase demonstrated Na^+ conductivity and facilitated redox reactions in full cells, suggesting that water exposure reduces coulombic attraction and enhances Na^+ migration within MnHCFe. Further analyses measured the distances between Na^+ ions and N^- in the CN^- ligands across different unit cells (Fig. 3d and e). Results indicated that ionic conductivity and activation energy are influenced by these distances; notably, the cubic structure, with the longest Na^+–N distances, exhibited the lowest activation energy and the highest Na^+ conductivity. This phenomenon likely results from weaker coulombic attractions due to a smaller concentration of Na^+ (1.04 mol) and a higher amount of H_2O (1.04 mol). Conversely, the rhombohedral structure, which has the shortest Na^+–N distances, showed the highest activation energy and the lowest Na^+ conductivity, correlating with its higher Na^+ content (approximately 1.5 mol) and lower water content (0.16 mol), resulting in stronger coulombic interactions. Additionally, all three MnHCFe phases conform to the Meyer–Neldel rule, as illustrated in Fig. 3f. This observation underscores that decreases in activation energy (E_a) are often accompanied by reductions in the conductivity prefactor (σ_0) in the Arrhenius rate law, highlighting the critical role of both the Arrhenius prefactor and E_a in ion conduction.[40–43] To validate our findings regarding the impact of Na^+ and anion interactions on conductivity, we performed bond valence energy landscape (BVEL) calculations (Fig. 3g–i). These calculations revealed activation energies for Na^+ migration of 0.168 eV for the cubic phase, 0.395 eV for the monoclinic phase, and 1.02 eV for the rhombohedral phase (Fig. 3j–m). The BVEL results align with our expectations, further confirming that Na^+ conductivity and the activation energy for Na^+ migration are fundamentally dependent on the interactions between Na^+ ions and the surrounding anions, which are influenced by the relative amounts of Na^+ and water in the MnHCFe structures.

DFT study of Na^+–CN^- interactions in representative structures

To elucidate the underlying mechanisms of observed variations in Na^+–N interactions across different phases of MnHCFe, we conducted a computational analysis using

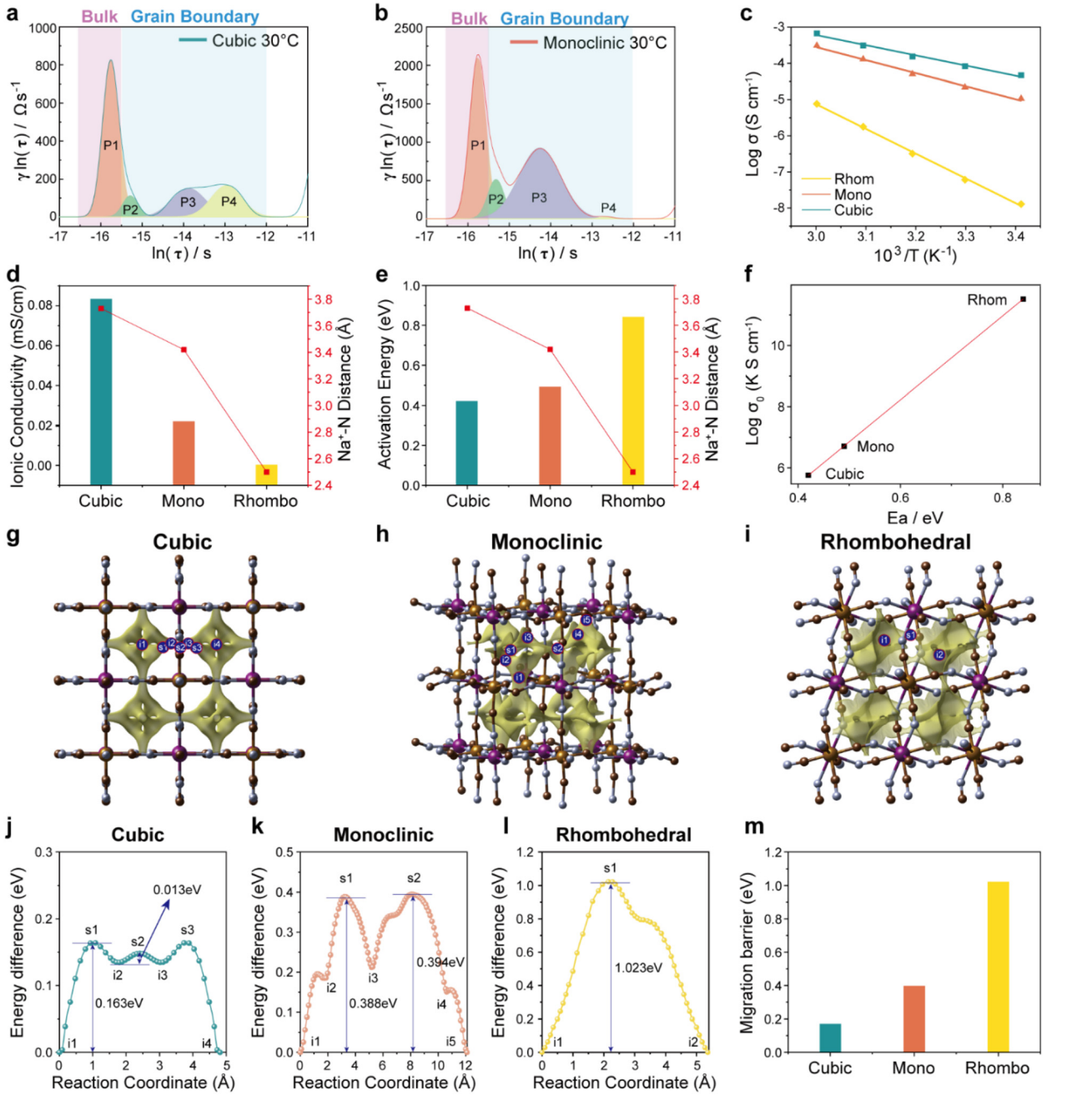

Fig. 3 Ionic conductivity of MnHCFe with different crystal structures. (a and b) Analysis of distribution of relaxation times for cubic (a) and monoclinic (b) phases, illustrating the contributions from bulk and grain boundary regions. (c) Arrhenius plots of the intrinsic bulk activation energy for Na^+ migration in MnHCFe. (d) Ionic conductivity and (e) activation energy of MnHCFe as a function of the Na^+–N distance for cubic, monoclinic, and rhombohedral phases. (f) Meyer–Neldal plots of log σ_0 *versus* activation energies, E_a, for three MnHCFe phases. (g–i) Isosurfaces of Na^+ transport channels in cubic, monoclinic, and rhombohedral MnHCFe structures, calculated using the bond valence energy landscape (BVEL) method. (j–l) Energy profiles along the migration paths in these three structures, calculated using the BVEL method. (m) Migration barrier for Na^+ ions across the three crystal structures (BVEL method).

density functional theory (DFT). This analysis revealed electronic changes corresponding to the structural differences in MnHCFe. We generated the structures of water-containing MnHCFe based on previous literature,[35,44] modeling them as $NaMn[Fe(CN)_6]\cdot H_2O$ for the cubic phase, $Na_2Mn[Fe(CN)_6]\cdot 2H_2O$ for the monoclinic phase, and $Na_2Mn[Fe(CN)_6]$ for the rhombohedral phase. These structures were fully relaxed using the GGA+*U* method (refer to the Computational details section for more information), and the results are displayed in Fig. 4a. Consistent with experimental observations, our computational studies confirmed that an increase in Na^+ content leads to bending in the Mn–N–C bonds, facilitating

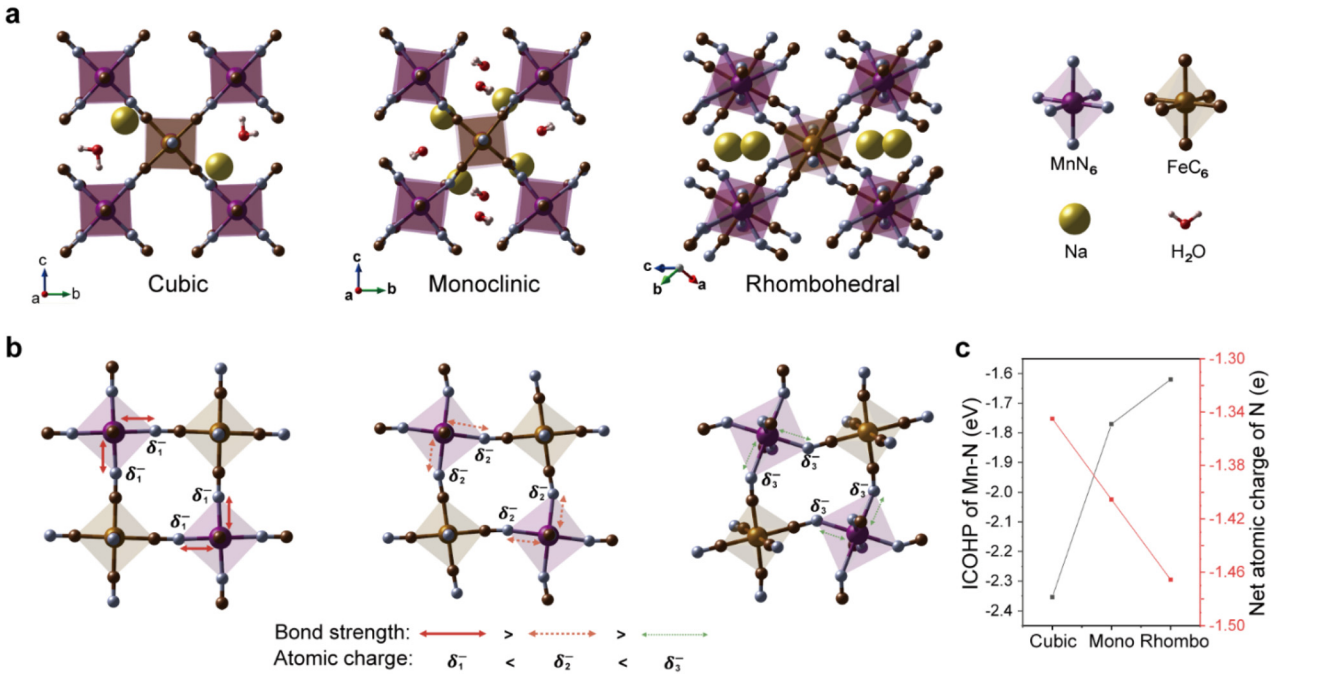

Fig. 4 Computational analysis of structural and electronic properties across different MnHCFe phases. (a) DFT-optimized structures of NaMn[Fe(CN)$_6$]·H$_2$O, Na$_2$Mn[Fe(CN)$_6$]·2H$_2$O, and Na$_2$Mn[Fe(CN)$_6$] for cubic, monoclinic, and rhombohedral phases, respectively. (b) Schematic illustrating the impact of phase transition on Mn–N bond strengths and nitrogen atomic charges. (c) Average ICOHP values for Mn–N bonds and atomic charges of nitrogen.

the transformation of the cubic MnHCFe into a monoclinic framework.[35] Moreover, the enhanced bending of Mn–N–C bond angles in the dehydrated rhombohedral MnHCFe contributes to the stabilization of this structure through bond distortion,[41] indicating a preference for stability *via* structural modifications. Further analysis involved the Integrated Crystal Orbital Hamilton Population (ICOHP) and Bader charge analysis to explore changes in the electronic structure induced by bond modifications across the phases.[45–48] As illustrated in Fig. 4b, these analyses depict the structural transition from cubic to monoclinic to rhombohedral phases. The results, shown in Fig. 4c, indicate a decrease in Mn–N bond strength—as reflected by reduced ICOHP values—and an increase in the atomic charge on nitrogen in a more negative direction. The decrease in Na^+ mobility can thus be partially attributed to the strengthened interaction between Na^+ and negatively charged nitrogen atoms.[49] This comprehensive study provides valuable insights into how Na^+ and H_2O contents influence the interactions between Na^+ and CN^- ligands, impacting Na^+ migration. These findings offer significant implications for the design of high-performing Na^+ conducting PBA materials, enhancing our understanding of the structural and electronic factors that govern ion transport in these systems.

Comparative electrochemical performance of ASNBs

To assess the impact of the crystal structure on cell performance, we conducted galvanostatic cycling with potential limitation (GCPL) measurements on the three MnHCFe phases using MnHCMn as the cathode and Na_3Sn as the anode. The voltage profiles of ASNBs using these MnHCFe phases are presented in Fig. 5a and b, in which cell redox behaviors are similar to the typical redox reactions of MnHCMn.[50] The rhombohedral phase does not demonstrate battery performance due to its low Na^+ conductivity. *Vice versa*, the ASNBs using cubic and monoclinic MnHCFe exhibit cycling performance over 30 cycles with two redox reactions (Mn(I)/Mn(II) and Mn(II)/Mn(III)), delivering initial capacities of 127 mAh g^{-1} and 120 mAh g^{-1}, respectively, which decrease to 15 mAh g^{-1} and 93 mAh g^{-1} after 30 cycles, operated in the cut-off voltage range of 0.9 V to 3.0 V at 30 °C and a 0.2C rate. Intriguingly, despite the cubic phase having faster Na^+ conductivity and lower activation energy, the monoclinic phase exhibits better capacity retention, demonstrating more stable performance (Fig. 5c). In the cubic MnHCFe cell (Fig. 5a), a soft breakdown occurred when the second plateau (~2.75 V) was accessed during charging, resulting in increased capacity and current exceeding the critical current density (CCD), compared to utilizing only the first plateau (~2 V). To investigate this behavior, electronic conductivity and CCD measurements were conducted.

Fig. S14 shows chronoamperometry data for Na^+-blocking SUS/MnHCFe/SUS symmetry cells with a voltage step of 0.2 V. The electronic conductivity was determined to be 1.4×10^{-8} S cm^{-1} for the cubic phase and 1.7×10^{-9} S cm^{-1} for the monoclinic phase (Fig. S14), which are sufficiently low to classify MnHCFe as a solid electrolyte, comparable to other sulfide

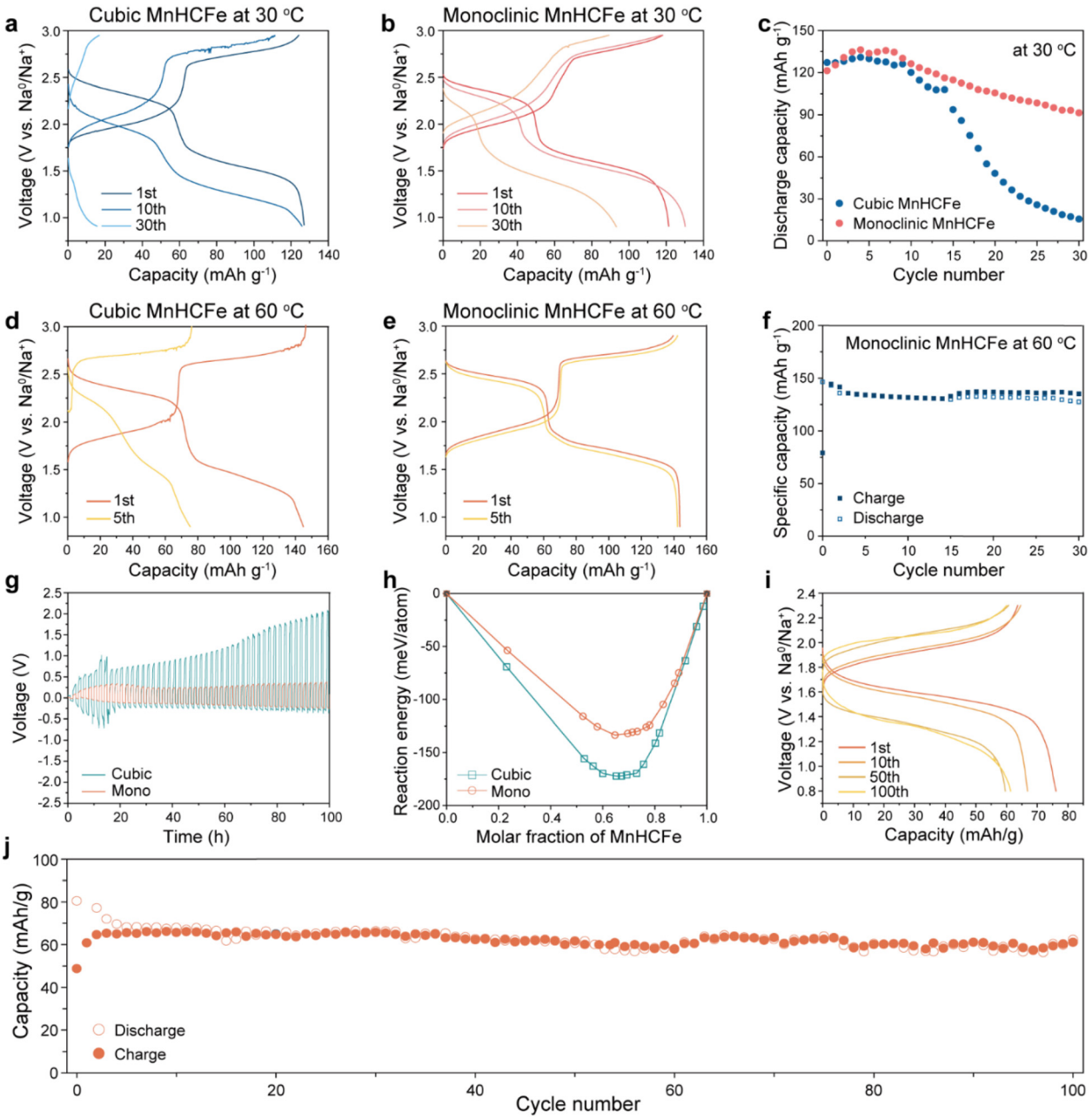

Fig. 5 Electrochemical performance and stability of Na_3Sn/MnHCFe/MnHCMn solid-state batteries. (a and b) Galvanostatic charge–discharge profiles of MnHCFe electrolytes for the (a) cubic and (b) monoclinic phases and their (c) cycling performance at 0.2C rate and 30 °C. (d and e) Galvanostatic charge–discharge profiles of MnHCFe electrolytes in the first and fifth cycles for the cubic (d) and monoclinic (e) phases at 0.2C rate and 60 °C. (f) Cycling performance of monoclinic MnHCFe at 0.2C rate and 60 °C. (g) Symmetric cell test using Na_3Sn electrodes with cubic and monoclinic MnHCFe electrolytes at 30 °C. (h) Calculated reaction energies of cubic and monoclinic MnHCFe phases with Na_3Sn as a function of the mixing ratio of MnHCFe. (i) Voltage profiles of full cells using the monoclinic MnHCFe electrolyte utilizing the Mn(I)/Mn(II) redox plateau of MnHCMn at 0.2C rate and room temperature. (j) Cyclability of the full cell using monoclinic MnHCFe at 0.2C rate and room temperature.

solid electrolytes.[51] The CCD and areal capacity for both phases were measured as 0.3 mA cm^{-2} and 0.3 mAh cm^{-2}, respectively (Fig. S15). Utilizing both redox plateaus of MnHCFe, which targets a capacity of 120 mAh g^{-1}, would result in a current density of 0.076 mA cm^{-2} and an areal capacity of 0.380 mAh cm^{-2}, exceeding the critical areal capacity. This likely induces soft breakdown and unstable cycling behavior when employing both redox plateaus of MnHCMn. In contrast, operating the cell within a stable voltage range and utilizing only the Mn(I)/Mn(II) redox plateau at a capacity of 70 mAh g^{-1} yields a current density of 0.038 mA cm^{-2} and an areal capacity of 0.190 mAh cm^{-2}, both well within the critical limits, resulting in stable cycling performance with minimal capacity fading.

To validate the two-plateau reactions, full cells of Na_3Sn/MnHCFe/MnHCMn were tested at 60 °C to increase ionic conductivity and mitigate soft breakdown. Both cubic and monoclinic phases initially delivered a discharge capacity of around 140 mAh g^{-1} at a 0.2C rate and at 60 °C as shown in Fig. 5d and e. However, the discharge capacity of the cubic phase decreased to about 80 mAh g^{-1} after 5 cycles, while the monoclinic phase maintained a similar capacity after 5 cycles. Since monoclinic electrolytes tend to improve cycling stability, ASNBs using monoclinic MnHCFe cycled with two redox reactions (Mn(I)/Mn(II) and Mn(II)/Mn(III)), delivering an initial capacity of 140 mAh g^{-1} and maintaining 130 mAh g^{-1} after 30 cycles (Fig. 5f). Nevertheless, the cyclability remains limited. To further explore the challenges associated with cycling performance, we conducted Na_3Sn symmetry cell tests at a current density of 0.05 mA cm^{-2} and at 30 °C for 100 h. As shown in Fig. 5g and summarized in Fig. S16, the monoclinic phase shows a lower overpotential of around 0.3 V than the 2 V for the cubic phase after 100 h, implying better stability with Na_3Sn. Furthermore, EIS measurements were taken every 10 hours and subsequently analyzed using DRT analysis during Na_3Sn symmetric cell tests at a current density of 0.05 mA cm^{-2} and at 25 °C for 100 h (Fig. S17 and S18). As shown in Fig. S18, the cubic phase shows a continuous increase in interfacial resistance due to SEI formation, whereas the monoclinic phase maintains stable interfacial resistance beyond 40 hours. DRT analysis further confirms that the increase in resistance during cycling arises primarily from SEI evolution, while the bulk and grain boundary resistances remain relatively unchanged. The stability appears to be the critical factor in the different cycle performances observed. The monoclinic phase, containing more Na^+ (1.5 mol), exhibits enhanced stability with Na_3Sn compared to the cubic phase with 1 mol of Na^+, likely due to the reduction in chemical potential differences between the anode and the solid electrolyte.[52] Our DFT calculations of reaction energies between Na_3Sn and the MnHCFe phases support this hypothesis (Fig. 5h and Tables S13 and S14). The cubic MnHCFe phase has a lower reaction energy (−171 meV) than the monoclinic MnHCFe phase (−133 meV), suggesting that a higher Na^+ content enhances the interfacial stability between Na_3Sn and MnHCFe. Consequently, the larger Na^+ content in the monoclinic phase contributes to its interfacial stability, making it the most effective solid electrolyte for ASNBs among the tested MnHCFe phases. This effectiveness is attributed to its adequate Na^+ conductivity and enhanced stability in full-cell configurations. Considering interfacial stability, the interface between the Na_3Sn anode and MnHCFe electrolyte represents a critical bottleneck for achieving stable two-plateau reactions. To further investigate the interfacial decomposition products formed due to parasitic reactions between the Na_3Sn anode and the MnHCFe electrolyte, *post-mortem* X-ray photoelectron spectroscopy (XPS) analyses of O 1s, C 1s, Mn 2p, and Fe 2p were conducted after symmetric Na_3Sn cell testing. The results and detailed discussion are provided in Fig. S19–S23 and Note S1.

In efforts to mitigate instability, ASNBs incorporating monoclinic MnHCFe were tested using the Mn(I)/Mn(II) redox reaction at a 0.2C rate and room temperature. As shown in Fig. 5i and j, the single plateau reaction maintained a discharge capacity of around 60 mAh g^{-1} after 100 cycles, indicating stable cycling performance with minimal capacity fading. These results underscore the importance of interfacial stability between Na_3Sn and MnHCFe in achieving stable cycling performance, which is also attributable to the optimized Na^+ and water content. Understanding the interplay between Na^+ and water contents was pivotal in achieving these outcomes. Na^+ content influences the coulombic interactions between Na^+ and nitrogen (N^-) in CN^- ligands, typically leading to reduced Na^+ conductivity at a Na^+ content of 1 as a threshold. Conversely, water content can mitigate these interactions by enhancing Pauli repulsion between Na^+ and the framework, thus facilitating faster Na^+ movement. An optimized Na^+ content of approximately 1 mol optimizes conductivity: a Na^+ content higher than 1 mol slows down conductivity due to increased coulombic interactions and lattice distortion, while too little Na^+ also diminishes conductivity due to a reduced number of mobile cations and smaller channel size. Appropriate water content further optimizes conductivity by reducing Na^+–N interactions. In terms of cell performance, increasing Na^+ content enhances interfacial stability between the PBA and the Na–Sn alloy, crucial for long-term cell stability and performance. This investigation into the effects of Na^+ and water content not only advances our understanding of PBA superionic conductors but also provides a robust framework for designing high-performance ASNBs. This approach, focusing on controlled Na^+ and water content, offers promising directions for enhancing the Na^+ conductivity and overall performance of PBA-based batteries.

Conclusion

In this study, we have investigated the influence of Na^+ and water content on the design and performance of PBA solid electrolytes for ASNBs. Our analysis focuses on Na^+ conductivity across three crystallographic phases of MnHCFe: cubic, monoclinic, and rhombohedral. Through ICP-MS, TGA, NPD, and XAFS analyses, we have found that the MnHCFe phases contain different amounts of Na^+ and water in the different crystal structures: the cubic phase containing 1.04 mol of Na^+ and 1.04 mol of water exhibited no lattice distortion. In contrast, the monoclinic phase, with 1.51 mol of Na^+ and 1.49 mol of water, showed slight lattice distortion, while the rhombohedral phase, with 1.51 mol of Na^+ and only 0.16 mol of water, exhibited significant lattice distortion. These structural changes are driven by the interactions between Na^+ and N^- in CN^- ligands, affecting the Na^+ conductivity due to the resultant lattice distortions. To further investigate the effects of Na^+ and water content on structural transitions and ionic conductivity, MnHCFe samples with

varying Na^+ concentrations, as well as gradually dehydrated MnHCFe, were characterized. Synchrotron XRD and Le Bail fitting revealed that both Na^+ content and water content play critical roles in determining the structure and ionic conductivity. An increase in Na^+ content enhances ionic conductivity in the cubic phase; however, once the Na^+ content exceeds approximately 1, a phase transition to the less conductive monoclinic phase occurs. Additionally, dehydration disrupts structural stability, inducing phase transitions and leading to a further reduction in ionic conductivity. To further quantify the effects on Na^+ conductivity, we conducted EIS, DRT analysis, and computational simulations *via* BVEL and DFT calculations. The Na^+ conductivities are 8.3×10^{-2} mS cm^{-1}, 2.2×10^{-2} mS cm^{-1}, and 6.1×10^{-5} mS cm^{-1} for the cubic (1.04 mol of Na^+ and 1.04 mol of water), monoclinic (1.51 mol of Na^+ and 1.49 mol of water), and rhombohedral phases (1.51 mol of Na^+ and 0.16 mol of water), respectively. Moreover, activation energies for Na^+ migration were calculated to be 0.42 eV for cubic, 0.49 eV for monoclinic, and 0.84 eV for rhombohedral structures, correlating inversely with the degree of lattice distortion. Based on these findings, we conclude that maintaining a cubic phase with approximately 1 mol of Na^+ ions and an adequate water content is critical for achieving high ionic conductivity. Adequate water content helps sustain the channel size and stabilize the cubic crystal phase, reducing coulombic interactions and enhancing Na^+ mobility. These optimized conditions offer a pathway to significantly enhance the ionic conductivity of PBAs by balancing mobile cation concentration and structural stability.

In terms of cell performance, the monoclinic MnHCFe has outperformed the other phases, demonstrating better cycling performance despite the cubic phase having faster Na^+ conductivity. In the case of stability, the interface between the Na_3Sn anode and the MnHCFe electrolyte can be the bottleneck. As a result, monoclinic MnHCFe was selected as the solid electrolyte for further ASNB applications. The assembled full cells exhibited robust performance, delivering a discharge capacity of 60 mAh g^{-1} at room temperature and at 0.2C rate over 100 cycles. This comprehensive study underscores the critical role of Na^+ and water content in enhancing Na^+ conductivity and optimizing cell performance in PBA-based ASNBs. By modulating the coulombic interactions between Na^+ ions and the CN^- ligands, we can significantly influence both the ionic transport and the structural stability of the electrolytes. Furthermore, increasing the Na^+ content not only improves the interface stability between the PBA and anode materials like Na–Sn alloy but also minimizes chemical potential differences, thereby enhancing cycling performance. These insights pave the way for the development of advanced PBA superionic conductors, offering promising strategies for the practical application of all-solid-state battery technologies. Our findings provide a robust framework for future research and development in the field, marking a significant advancement in the understanding and application of PBA materials in energy storage systems.

Author contributions

T. K., Y.-Y. S., and S. R. contributed equally to this work. T. K., S. R., and H.-W. L. conceived the idea and designed the experiments. D.-H. S., S.-K. J., and H.-W. L. supervised the project. T. K. and S. R. performed characterization, carried out electrochemical measurements and analyzed the data. Y.-Y. S. and D.-H. S. performed DFT simulations. S. H. A., B. J. P., C. L., and M.-H. K. assisted in characterization. T. K., Y.-Y. S., S. R., D.-H. S., S.-K. J., and H.-W. L. wrote the manuscript. All coauthors revised and commented on the manuscript.

Conflicts of interest

There are no conflicts to declare.

Data availability

The data supporting this article have been included as part of the SI.

SI, including experimental procedures, supplementary figures (Fig. S1–S23), tables (Tables S1–S14), and a supplementary note, is available. See DOI: https://doi.org/10.1039/d5eb00129c.

Acknowledgements

This work was supported by the National Research Foundation of Korea (NRF) (RS-2024-00428511, RS-2024-00435493, and RS-2023-00208929), KIST Institutional Program (No. 2E31861), and National Research Council of Science & Technology (NST) grant of the Korea Government (MSIT) (No. GTL24011-000). The computational work was supported by the Supercomputing Center/Korea Institute of Science and Technology Information with supercomputing resources including technical support (KSC-2022-CRE-0343 to H.-W. L.). The XANES, EXAFS, and synchrotron XRD experiments were performed at beamline 6D of the Pohang Accelerator Laboratory (PAL). The neutron powder diffraction experiment was conducted at the HANARO facility at the Korea Atomic Energy Research Institute (KAERI). This study contains the results obtained by using the equipment of UNIST Central Research Facilities (UCRF).

References

1 R. Usiskin, Y. Lu, J. Popovic, *et al.*, Fundamentals, status and promise of sodium-based batteries, *Nat. Rev. Mater.*, 2021, **6**, 1020–1035.
2 Z. Zhu, T. Jiang, M. Ali, *et al.*, Rechargeable batteries for grid scale energy storage, *Chem. Rev.*, 2022, **122**, 16610–16751.

3 J. E. Jang, R.-A. Kim, S. Jayasubramaniyan, *et al.*, Full-Hexacyanometallate aqueous redox flow batteries exceeding 1.5 V in an aqueous solution, *Adv. Energy Mater.*, 2023, **13**, 202300707.
4 J. E. Jang, S. Jayasubramaniyan, S. W. Lee and H. W. Lee, A hexacyanomanganate negolyte for aqueous redox flow batteries, *ACS Energy Lett.*, 2023, **8**, 3702–3709.
5 T. Jiang, D. Shen, Z. Zhang, *et al.*, Battery technologies for grid-scale energy storage, *Nat. Rev. Clean Technol.*, 2025, **1**, 474–492.
6 Z. Zhu, T. Jiang, M. Ali, *et al.*, Rechargeable Batteries for Grid Scale Energy Storage, *Chem. Rev.*, 2022, **122**(22), 16610–16751.
7 E. A. Wu, S. Banerjee, H. Tang, *et al.*, A stable cathode-solid electrolyte composite for high-voltage, long-cycle-life solid-state sodium-ion batteries, *Nat. Commun.*, 2021, **12**, 1256.
8 J. Yang, G. Liu, M. Avdeev, *et al.*, Ultrastable all-solid-state sodium rechargeable batteries, *ACS Energy Lett.*, 2020, **5**, 2835–2841.
9 J. Park, D. Han, J. P. Son, *et al.*, Extending the electrochemical window of Na^+ halide nanocomposite solid electrolytes for 5 V-class all-solid-state Na-ion batteries, *ACS Energy Lett.*, 2024, **9**, 2222–2230.
10 T. Kim, S. H. Ahn, Y. Y. Song, *et al.*, Prussian blue-type sodium-ion conducting solid electrolytes for all solid-state batteries, *Angew. Chem., Int. Ed.*, 2023, **62**, e202309852.
11 J. E. Lee, K. H. Park, J. C. Kim, *et al.*, Universal solution synthesis of sulfide solid electrolytes using alkahest for all-solid-state batteries, *Adv. Mater.*, 2022, **34**, 202200083.
12 C. Lee, T. U. Wi, W. Go, *et al.*, Unveiling interfacial dynamics and structural degradation of solid electrolytes in a seawater battery system, *J. Mater. Chem. A*, 2020, **8**, 21804–21811.
13 T. U. Wi, C. Lee, M. F. Rahman, *et al.*, Chemical stability and degradation mechanism of solid electrolytes/aqueous media at a steady state for long-lasting sodium batteries, *Chem. Mater.*, 2021, **33**, 126–135.
14 T. Famprikis, P. Canepa, J. A. Dawson, *et al.*, Fundamentals of inorganic solid-state electrolytes for batteries, *Nat. Mater.*, 2019, **18**, 1278–1291.
15 C. Lee, J. Y. Kim, K. Y. Bae, *et al.*, Enhancing electrochemo-mechanics: How stack pressure regulation affects all-solid-state batteries, *Energy Storage Mater.*, 2024, **66**, 103196.
16 J. Janek and W. G. Zeier, Challenges in speeding up solid-state battery development, *Nat. Energy*, 2023, **8**, 230–240.
17 L. Zhou, T. T. Zuo, C. Y. Kwok, *et al.*, High areal capacity, long cycle life 4 V ceramic all-solid-state Li-ion batteries enabled by chloride solid electrolytes, *Nat. Energy*, 2022, **7**, 83–93.
18 J. Jayasubramaniyan, C. Lee, H. W. Lee, *et al.*, Progress and perspectives of space charge limited current models in all-solid-state batteries, *J. Mater. Res.*, 2022, **37**, 4017–4034.
19 C. Lee, S. Y. Han, J. A. Lewis, *et al.*, Stack pressure measurements to probe the evolution of the lithium-solid-state electrolyte interface, *ACS Energy Lett.*, 2021, **6**, 3261–3269.
20 Z. Yang, B. Tang, Z. Xie, *et al.*, NASICON-type $Na_3Zr_2Si_2PO_{12}$ solid-state electrolytes for sodium batteries, *ChemElectroChem*, 2021, **8**, 1035–1047.
21 A. Banerjee, K. H. Park, J. W. Heo, *et al.*, Na_3SbS_4: A solution processable sodium superionic conductor for all-solid-state sodium-ion batteries, *Angew. Chem., Int. Ed.*, 2016, **55**, 9634–9638.
22 T. W. Kim, K. H. Park, Y. E. Choi, J. Y. Lee and Y. S. Jung, Aqueous-solution synthesis of Na_3SbS_4 solid electrolytes for all-solid-state Na-ion batteries, *J. Mater. Chem. A*, 2018, **6**, 840–844.
23 K. H. Kwak, J. Lyoo, J. Park, *et al.*, Na_2ZrCl_6 enabling highly stable 3 V all-solid-state Na-ion batteries, *Energy Storage Mater.*, 2021, **37**, 47–54.
24 K. H. Kwak, D. Han, J. Lyoo, *et al.*, New cost-effective halide solid electrolytes for all-solid-state-batteries: Mechanochemically prepared Fe^{3+}-substituted Li_2ZrCl_6, *Adv. Energy Mater.*, 2021, **11**, 2003190.
25 A. Hayashi, K. Noi, A. Sakuda and M. Tatsumisago, Superionic glass-ceramic electrolytes for room-temperature rechargeable sodium batteries, *Nat. Commun.*, 2012, **3**, 856.
26 J.-F. Wu, Q. Wang and X. Guo, Sodium-ion conduction in $Na_2Zn_2TeO_6$ solid electrolytes, *J. Power Sources*, 2018, **402**, 513–518.
27 K. H. Kwak, S. Wang, J. Park, *et al.*, Emerging halide superionic conductors for all-solid-state batteries: Design, synthesis, and practical applications, *ACS Energy Lett.*, 2022, **7**, 1776–1805.
28 J.-F. Wu, R. Zhang, Q.-F. Fu, *et al.*, Inorganic solid electrolytes for all-solid-state sodium batteries: Fundamentals and strategies for battery optimization, *Adv. Funct. Mater.*, 2021, **31**, 2008165.
29 K. H. Park, Q. Bai, D. H. Kim, *et al.*, Design strategies, practical considerations, and new solution processes of sulfide solid electrolytes for all-solid-state batteries, *Adv. Energy Mater.*, 2018, **8**, 1800035.
30 P. K. Pathak, K. P. Agrim, C. Park, H. Ahn and R. R. Salunkhe, Elevating the performance of the Prussian Blue analogue cathode for sodium-ion batteries by adjusting the low spin Fe redox, *ACS Appl. Energy Mater.*, 2024, **7**, 11352–11360.
31 A. Choi, Y.-Y. Song, J. Kim, *et al.*, Enhancing efficiency of low-grade heat harvesting by structural vibration entropy in thermally regenerative electrochemical cycles, *Adv. Mater.*, 2023, **35**, 2303199.
32 D. Kim, A. Choi, C. Park, M. H. Kim and H. W. Lee, Investigating the role of interstitial water molecules in copper hexacyanoferrate for sodium-ion battery cathodes, *J. Mater. Chem. A*, 2023, **11**, 13535–13542.
33 A. Mullaliu, J. Asenbauer, G. Aquilanti, S. Passerini and M. Giorgetti, Highlighting the reversible manganese electroactivity in Na-rich manganese hexacyanoferrate material for Li- and Na-ion storage, *Small Methods*, 2020, **4**, 1900529.
34 L. Deng, J. Qu, X. Niu, *et al.*, Defect-free potassium manganese hexacyanoferrate cathode material for high-perform-

ance potassium-ion batteries, *Nat. Commun.*, 2021, **12**, 2167.

35 P. Xiao, J. Song, L. Wang, J. B. Goodenough and G. Henkelman, Theoretical study of the structural evolution of a $Na_2FeMn(CN)_6$ cathode upon Na intercalation, *Chem. Mater.*, 2015, **27**, 3763–3768.

36 W. Wang, Y. Gang, Z. Hu, *et al.*, Reversible structural evolution of sodium-rich rhombohedral Prussian blue for sodium-ion batteries, *Nat. Commun.*, 2020, **11**, 980.

37 M. Qin, W. Ren, R. Jiang, Q. Li, X. Yao, S. Wang, Y. You and L. Mai, Highly crystallized Prussian blue with enhanced kinetics for highly efficient sodium storage, *ACS Appl. Mater. Interfaces*, 2021, **13**, 3999–4007.

38 P. Braun, C. Uhlmann, A. Weber, H. Störmer, D. Gerthsen and E. Ivers-Tiffée, Separation of the bulk and grain boundary contributions to the total conductivity of solid lithium-ion conducting electrolytes, *J. Electroceram.*, 2017, **38**, 157–167.

39 T. H. Wan, M. Saccoccio, C. Chen and F. Ciucci, Influence of the discretization methods on the distribution of relaxation times deconvolution: Implementing radial basis functions with DRTtools, *Electrochim. Acta*, 2015, **184**, 483–497.

40 S. Muy, J. C. Bachman, H.-H. Chang, *et al.*, Lithium conductivity and Meyer-Neldel rule in Li_3PO_4-Li_3VO_4-Li_4GeO_4 lithium superionic conductors, *Chem. Mater.*, 2018, **30**, 5573–5582.

41 S. Muy, R. Schlem, Y. Shao-Horn and W. G. Zeier, Phonon-ion interactions: Designing ion mobility based on lattice dynamics, *Adv. Energy Mater.*, 2021, **11**, 2002787.

42 S. P. Culver, R. Koerver, T. Krauskopf and W. G. Zeier, Designing ionic conductors: The interplay between structural phenomena and interfaces in thiophosphate-based solid-state batteries, *Chem. Mater.*, 2018, **30**, 4179–4192.

43 R. Jalem, A. Hayashi, F. Tsuji, A. Sakuda and Y. Tateyama, First-principles calculation study of Na^+ superionic conduction mechanism in W- and Mo-doped Na_3SbS_4 solid electrolytes, *Chem. Mater.*, 2020, **32**, 8373–8381.

44 X. Guo, Z. Wang, Z. Deng, *et al.*, Water contributes to higher energy density and cycling stability of Prussian blue analogue cathodes for aqueous sodium-ion batteries, *Chem. Mater.*, 2019, **31**, 5933–5942.

45 V. L. Deringer, A. L. Tchougréeff and R. Dronskowski, Crystal orbital Hamilton population (COHP) analysis as projected from plane-wave basis sets, *J. Phys. Chem. A*, 2011, **115**, 5461–5466.

46 R. Dronskowski and P. E. Blöchl, Crystal orbital Hamilton populations (COHP): Energy-resolved visualization of chemical bonding in solids based on density-functional calculations, *J. Phys. Chem.*, 1993, **97**, 8617–8624.

47 S. Maintz, V. L. Deringer, A. L. Tchougréeff and R. Dronskowski, Analytic projection from plane-wave and PAW wavefunctions and application to chemical-bonding analysis in solids, *J. Comput. Chem.*, 2013, **34**, 2557–2567.

48 M. Yu and D. R. Trinkle, Accurate and efficient algorithm for Bader charge integration, *J. Chem. Phys.*, 2011, **134**, 064111.

49 S. P. Culver, A. G. Squires, N. Minafra, *et al.*, Evidence for a solid-electrolyte inductive effect in the superionic conductor $Li_{10}Ge_{1(-x}Sn_xP_2S_{12}$, *J. Am. Chem. Soc.*, 2020, **142**, 21210–21219.

50 H. W. Lee, R. Y. Wang, M. Pasta, S. W. Lee, N. Liu and Y. Cui, Manganese hexacyanomanganate open framework as a high-capacity positive electrode material for sodium-ion batteries, *Nat. Commun.*, 2014, **5**, 5280.

51 A. Hayashi, N. Masuzawa, S. Yubuchi, *et al.*, A sodium-ion sulfide solid electrolyte with unprecedented conductivity at room temperature, *Nat. Commun.*, 2019, **10**, 5266.

52 S. K. Jung, H. Gwon, H. Kim, *et al.*, Unlocking the hidden chemical space in cubic-phase garnet solid electrolyte for efficient quasi-all-solid-state lithium batteries, *Nat. Commun.*, 2022, **13**, 7638.